INTERNATIONAL JOURNAL FOR NUMERICAL METHODS IN FLUIDS
Int. J. Numer. Meth. Fluids **29**: 451–464 (1999)

REYNOLDS STRESS MODELLING OF JET AND SWIRL INTERACTION INSIDE A GAS TURBINE COMBUSTOR

J.M. TSAO AND C.A. LIN*
Department of Power Mechanical Engineering, National Tsing Hua University, Hsinchu, 30043 Taiwan

SUMMARY

Influences of the inlet swirl levels on the interaction between the dilution air jets and the swirling cross-flow to the interior flow field inside a gas turbine combustor were investigated numerically by Reynolds stress transport model (RSTM). Due to the intense swirl and jet interaction, a high level of swirl momentum is transported to the centreline and hence, an intense vortex core is formed. The strength of the centreline vortex core was found to depend on the inlet swirl levels. For the higher swirling inlet, the decay of the swirling motion causes strong streamline variation of pressure; and consequently leads to an elevated level of deceleration of its axial velocity. Predictions contrasted with measurements indicate that the stress model reproduces the flow correctly and is able to reflect the influences of inlet swirl levels on the interior flow structure. Copyright © 1999 John Wiley & Sons, Ltd.

KEY WORDS: three-dimensional flow; turbulence modelling; incompressible fluid; swirl; gas turbine combustor

1. INTRODUCTION

Gas turbine combustor forms one of the key components in the jet engine assembly and other industrial devices. Current trends in designing gas turbine combustion chambers aim at improved performance, better combustion stability and efficiency, more uniform temperature at the chamber exit, low pollutant emissions and longer operation life. All are highly sensitive to details in the combustor flow structure, and there is a clear need for an accurate description of, and insight into, the flow conditions inside the combustor.

Swirling motion is often employed as a mechanism to further promote or control mixing between the fuel spray jet and the adjacent air, and, on some occasions, to stabilise the combustion zone due to the presence of the swirl-induced central recirculation zone. Although reaction and consequent heat release and density variations have profound effects on the flow details, gross features are dictated primarily by geometric constraints, the intensity and profiles of inlet swirl and the aerodynamics of the interaction between the dilution jets and the swirling chamber flow.

Since the decay of the swirl-induced central recirculation zone has profound effects on flame stabilisation and mixing in combustion systems, a prior knowledge of the flow characteristics is beneficial during the design process. Extensive computational studies have, therefore, been directed to the gas turbine combustor flow, which is three-dimensional in nature. These include

---

* Correspondence to: Department of Power Mechanical Engineering, National Tsing Hua University, Hsinchu, 30043 Taiwan.

CCC 0271–2091/99/040451–14$17.50

Received October 1997
Revised January 1998

can-type combustor [1–3] and annular-type combustor [4,5]. Resolving the predicted injection flow field relies heavily on the representation of turbulence and the accuracy of the numerical scheme approximating transport.

Previous numerical studies [1,4,5] indicated that the predicted chamber temperature was too high and the high temperature region was also mislocated in contrast to measurements, and these were attributed to the weakness of the eddy viscosity model adopted to represent the complex turbulent mixing mechanism. These predictive defects had led to limited attempts to adopt Reynolds stress closure for such flows [6,7]. In most combustor flows, however, due to the lack of complete experimental data, no measured turbulence quantities were available for comparisons to gain further insights of the turbulent transport processes.

Previous studies [6,7] indicated that the flow structure inside the combustor was dominated by the representation of the turbulent diffusive transport. However, in the cases studied [6,7], the amount of the swirl momentum transported into the combustor interior was low, the flow field being dictated by the colliding air jets, and hence the influences of swirl were modest. The present study focuses primarily on the influences of the elevated swirl level on the internal flow field. Due to the intense swirl and jet interaction, a high level of swirl momentum is transported to the centreline, and hence an intense vortex core is formed. The decay of swirling motion causes strong streamline variation of pressure; and consequently leads to a deceleration of its axial velocity. Therefore, effects of the decay of swirl-induced adverse and favourable pressure gradients on the flow structure are to be addressed computationally, and the simulations also serve to assess the stress model's predictive capabilities in this physical environment. Detail comparisons of the predicted results and measurements will be presented.

2. THE COMPUTATIONAL MODEL

2.1. The governing equations

With Φ denoting the linear momentum components U, V or the swirl component rW, these being directed in the respective orthogonal co-ordinates ξ, η, θ, as shown in Figure 1, the variation of Φ may, for high Reynolds number flow, be described by the equation:

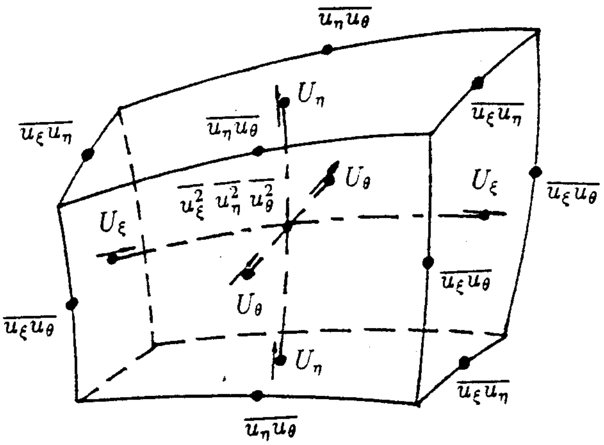

Figure 1. Staggered velocity and stress arrangement.

$$\frac{\partial}{\partial t}(\rho\Phi)+\frac{\partial}{\partial \xi}(\rho h_\eta rU\Phi)+\frac{\partial}{\partial \eta}(\rho h_\xi rV\Phi)+\frac{\partial}{\partial \theta}(\rho h_\xi h_\eta W\Phi)+\frac{\partial}{\partial \xi}(\rho h_\eta r\overline{u\phi})+\frac{\partial}{\partial \eta}(\rho h_\xi r\overline{v\phi})$$
$$+\frac{\partial}{\partial \theta}(\rho h_\xi h_\eta\overline{w\phi})=h_\xi h_\eta rS_\Phi, \qquad (1)$$

where $\overline{u\phi}$, $\overline{v\phi}$ and $\overline{w\phi}$ are turbulent fluxes; h_ξ, h_η and r are the metric coefficients and S_Φ is the source term related to Φ and collecting all fragments not accounted for by the explicit convection or diffusion terms. The continuity equation arises upon setting $\Phi = 1$ and nullifying the time derivative, the source and the diffusion terms.

In the present application, turbulence is described either by the high Reynolds number k–ϵ eddy viscosity model, used here merely as a datum closure, or by one of high Reynolds number stress closures, as detailed below, all involving six equations for the independent stresses $\overline{u_iu_j}$ and a seventh equation for the isotropic turbulence energy dissipation ϵ.

The Reynolds stress closure will be expressed in a general form, and this may be written as (in Cartesian tensor form):

$$\frac{\partial}{\partial x_k}(\rho U_k\overline{u_iu_j})=\frac{\partial}{\partial x_k}\left[\frac{\mu_t}{\sigma_k}\frac{\partial\overline{u_iu_j}}{\partial x_k}\right]\underbrace{-\rho\overline{u_iu_k}\frac{\partial U_j}{\partial x_k}-\rho\overline{u_ju_k}\frac{\partial U_i}{\partial x_k}}_{P_{ij}}+\epsilon_{ij}+\phi_{ij}, \qquad (2)$$

where $-\frac{2}{3}\rho\delta_{ij}\epsilon$ models stress dissipation ϵ_{ij} on the assumption that this process is isotropic and may thus be characterised by the dissipation of turbulence energy ϵ. The term ϕ_{ij} identifies the pressure/strain interaction and consists of three model components, representing respectively, 'return to isotropy', 'isotropisation of mean strain and turbulence correlation' and redistributive effects arising from wall reflection of pressure fluctuations.

The variant adopted is that of Gibson and Launder [8], and this may be written as:

$$\phi_{ij1}=-1.8\rho\frac{\epsilon}{k}\left[\overline{u_iu_j}-\frac{\delta_{ij}}{3}\overline{u_ku_k}\right], \qquad (3)$$

$$\phi_{ij2}=-0.6\left[P_{ij}-\frac{\delta_{ij}}{3}P_{kk}\right], \qquad (4)$$

$$\phi_{ijw}=0.5\rho\frac{\epsilon}{k}\left[\overline{u_ku_m}\boldsymbol{n}_k\boldsymbol{n}_m\delta_{ij}-\frac{3}{2}\overline{u_ku_i}\boldsymbol{n}_k\boldsymbol{n}_j-\frac{3}{2}\overline{u_ku_j}\boldsymbol{n}_k\boldsymbol{n}_i\right]f$$
$$+0.3\left[\phi_{km2}\boldsymbol{n}_k\boldsymbol{n}_m\delta_{ij}-\frac{3}{2}\phi_{ik2}\boldsymbol{n}_k\boldsymbol{n}_j-\frac{3}{2}\phi_{jk2}\boldsymbol{n}_k\boldsymbol{n}_i\right]f, \qquad (5)$$

where $\boldsymbol{n}_i$ is the wall normal unit vector in the direction i and $f=C_\mu^{0.75}k^{1.5}/(\epsilon\kappa y)$ with y being the distance to the closest wall, taken along the co-ordinate line normal to the wall.

The rate of turbulence energy dissipation, ϵ, appearing in the stress equations is determined from its own transport equation. The variant adopted here is that proposed by Craft and Launder [9], where the dissipation process is sensitised to anisotropy invariants, which takes the form,

$$\frac{\partial}{\partial x_k}(\rho U_k\epsilon)=\frac{\partial}{\partial x_k}\left[\frac{\mu_t}{\sigma_\epsilon}\frac{\partial\epsilon}{\partial x_k}\right]+\frac{\epsilon}{k}\left[0.35\left(P_k+\mu_t\left(\frac{\partial U_i}{\partial x_j}\right)^2\right)-\frac{1.92\epsilon}{1+1.65\sqrt{A_2}\,A}\right], \qquad (6)$$

where the invariants are given by $A_2=a_{ij}a_{ij}$, $A=1-\frac{9}{8}(A_2-A_3)$ and $A_3=a_{ij}a_{jk}a_{ki}$; with $a_{ij}=(\overline{u_iu_j}/k-\frac{2}{3}\delta_{ij})$. The adoption of this variant is motivated by the fact the standard form produced a too high level of jet penetration in the near-field [6,9].

2.2. Numerical algorithm

This scheme solves discretised versions of all equations over a staggered finite volume arrangement. As seen in Figure 1, a staggered storage is adopted not only for the velocity components but also for the shear stresses—an arrangement that aids stability by ensuring a strong numerical coupling between stresses and primary strains. The principle of mass–flux continuity is imposed indirectly via the solution of pressure-correction equations according to the SIMPLE algorithms [10]. The flow property values at volume faces contained in the convective fluxes that arise from the finite volume integration process, are approximated by the quadratic upstream-weighted interpolation scheme QUICK [11]. It should be pointed out that this scheme is applied to the momentum equations only. The adoption of the QUICK scheme would create five points stencil in each direction, with two points upstream and two points downstream of the control volume considered. The points neighbouring the control volume are treated implicitly, while the rest of the points are computed explicitly.

For turbulence model transport equations, especially the turbulent kinetic energy, dissipation rate and the normal stress equations, the adoption of the QUICK scheme may produce non-physical negative values of the transported properties. Therefore, the hybrid scheme is used in the turbulence model equations to ensure bounded solutions. The defect of the adoption of a lower-order convection scheme in the turbulence model equations are partly alleviated by the fact that theses equations are dominated by generation and destruction terms. Also, the adoption of eddy diffusivity to model the turbulent diffusion term reduces the values of the Peclet number, and this favours the hybrid scheme to remain within the centre differencing regime.

Though the present case is a steady state solution, it was found that using a time marching process will enhance stability, especially when stress models are employed. The solution process consists of a sequential algorithm in which each of the 11 sets of equations, in linearised form, is solved separately by the application of an alternate direction tridiagonal line-implicit solver. The number of ADI sweeps adopted in each equation is five, except in the pressure correction equation, in which the number of sweep employed is ten.

Convergence was judged by monitoring the magnitude of the absolute residual sources of mass and momentum, normalised by the respective inlet fluxes. The solution was taken as having converged when all above residuals fell below 0.01%.

The solution procedure may be summarised as follows:

1. initialise the variables;
2. solve U momentum equation;
3. solve V momentum equation;
4. solve rW momentum equation;
5. solve pressure correction equation:
    - update pressure
    - update velocities
6. solve Reynolds stress $\overline{u_i u_j}$ equations;
7. solve turbulence dissipation rate equation;
8. follow steps 2–7 until the specified convergence criteria are reached.

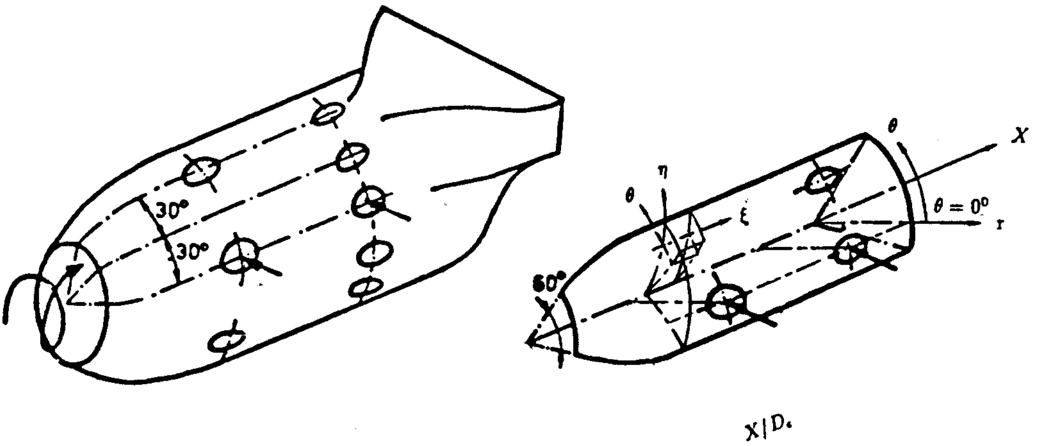

Figure 2. Geometry of gas turbine combustor model.

3. GEOMETRY AND BOUNDARY CONDITIONS

The geometry of the model combustor is shown in Figure 2. This consists of a hemispherical head section with a swirler inlet. The central part accommodates two rows of equally spaced jets. The first row consists of six primary jets, and the second row of 12 dilution jets. The numerical solution approximates the round injection holes by equal-area square orifices. Preliminary studies indicate that the results differ marginally with those adopting round-shaped holes. Predictions presented below focus on cases in which the mass flow rates from the inlet, primary jets and dilution jets are respectively, 20, 30 and 50% of the total discharge through the chamber outlet. The Reynolds number based on the bulk exit velocity and combustor diameter is 60000.

For an annular vaned swirler assuming uniform profiles [12], the swirl number can be approximated by

$$S=\frac{2}{3}\left[\frac{1-(d_{\mathrm{h}}/d)^3}{1-(d_{\mathrm{h}}/d)^2}\right]\tan\theta, \tag{7}$$

where θ is the swirl vane angle, and d and d_{h} are nozzle and vane pack hub diameters respectively. The vane angle of the two swirlers is 45°, with 18 and 20 vanes for swirler 1 and swirler 2 respectively. From the above formulation, the inlet swirl numbers, based on the geometrical characteristics of the swirlers given by Koutmos [13], are 0.74 and 0.85 for swirlers 1 and 2 respectively. The predicted results are contrasted with measurements by Koutmos, along the cross-section containing primary and dilution jets.

As seen in Figure 2, the 3D experimental domain is not, geometrically, axisymmetric, and therefore cannot be meshed by the present polar-cylindrical/curved-orthogonal approach. The experimental data suggest, however, that the 'swan-neck' exit section does not introduce significant distortions to flow upstream of the second row of dilution jets. It is this upstream part of the domain to which the present algorithm has been applied. Also, because of the circumferentially periodical arrangement of the dilution jets, only the 60° segment, shown in Figure 2, needed to be computed, with periodic boundary conditions applied in an implicit fashion at the segment's side. As seen in Figure 2, the co-ordinates, X, r and θ are the axial, radial and circumferential directions respectively.

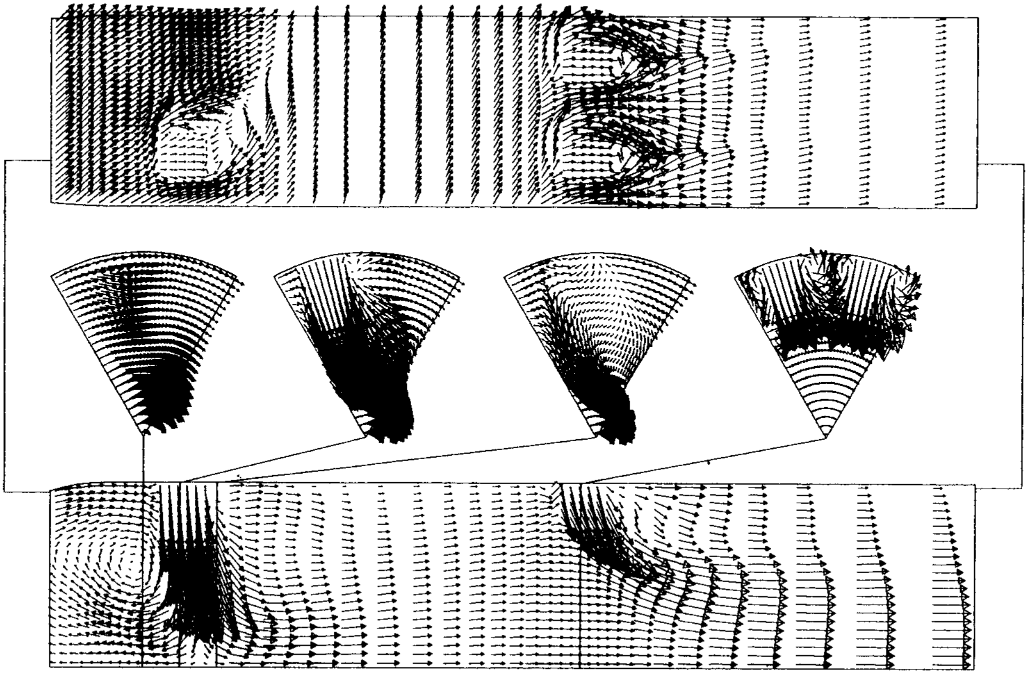

Figure 3. Overall view of the combustor flow—swirler 1.

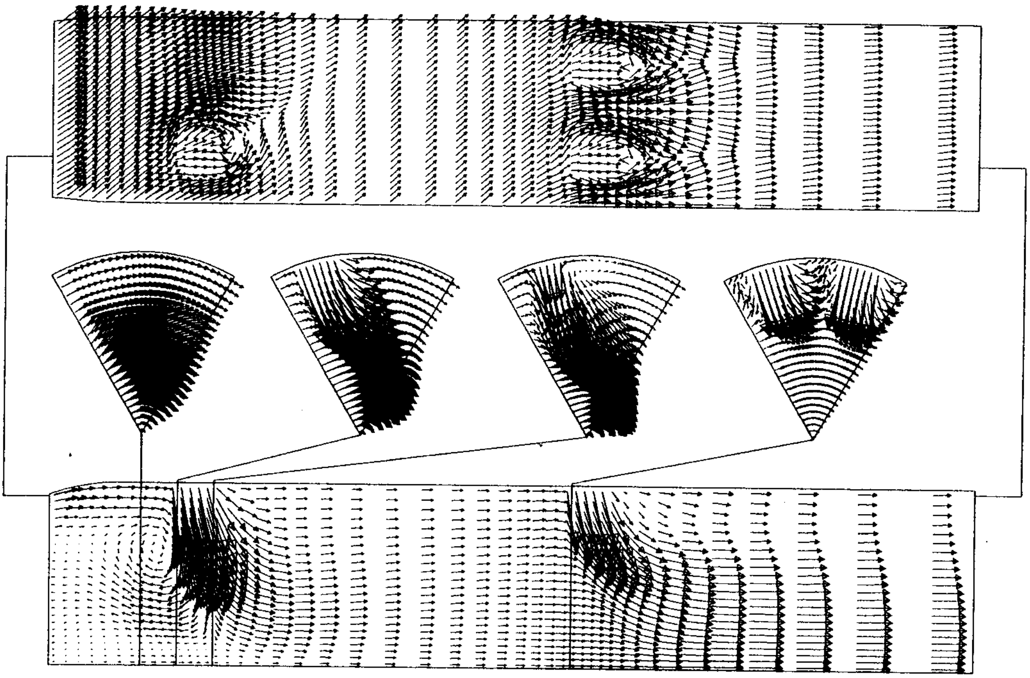

Figure 4. Overall view of the combustor flow—swirler 2.

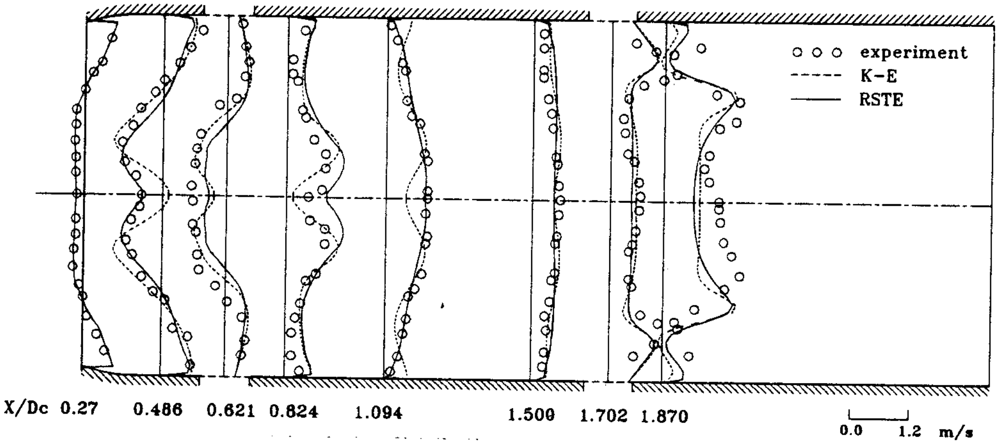

Figure 5. Predicted axial velocity—swirler 1.

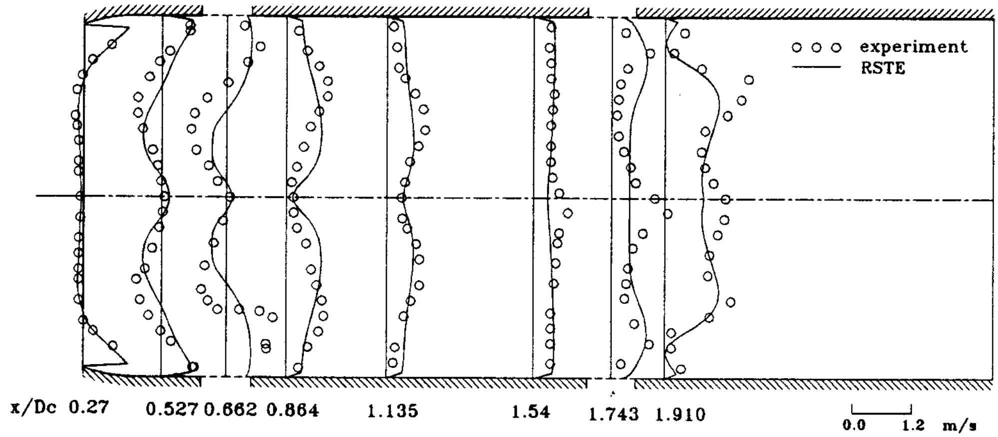

Figure 6. Predicted axial velocity—swirler 2.

The treatment at the axis of symmetry simply involved the prescription zero gradient conditions for all quantities except radial velocity and shear stresses, which were set to zero. Zero streamwise gradient conditions were prescribed along the computational outlet plane. Since no measured data are available at the swirler exit, the domain boundary at the swirler side was placed at the first leftmost location at which experimental data are available. Finally, the level of turbulence dissipation was obtained by using $\epsilon_{\text{in}} = k_{\text{in}}^{1.5}/L$, where L was chosen to be a quarter of the inlet jet radius.

At the combustor wall, the wall-parallel velocity components U and W were assumed to vary logarithmically between the semi-viscous sublayer, at $y_{\text{v}}^{+} = 11.2$, and the first computational node, P, lying in the region $30 < y^{+} < 100$. This treatment yielded boundary conditions for the shear stresses, i.e.

$$\overline{uv} = -\frac{C_{\mu}^{1/4} k_{\text{P}}^{1/2} \kappa}{\ln(E y_{\text{P}}^{+})} U_{\text{P}} \qquad \overline{vw} = -\frac{C_{\mu}^{1/4} k_{\text{P}}^{1/2} \kappa}{\ln(E y_{\text{P}}^{+})} W_{\text{P}}.$$

The dominant terms of the near-wall generation rates of the tangential normal stresses were recomputed over the associated near-wall finite volumes by assuming a constant shear stress and logarithmical variation of the velocity, i.e.

$$\iiint_{\mathrm{vol}} -\rho\overline{uv}\,\frac{\partial U}{\partial y}\,\mathrm{d}v = \frac{1}{y_{\mathrm{n}}}\int_{y_{\mathrm{v}}}^{y_{\mathrm{n}}} -\rho\overline{uv}\,\frac{\partial U}{\partial y}\,\mathrm{d}y\ \mathrm{vol} = \frac{1}{y_{\mathrm{n}}}\,\frac{\rho\overline{uv}^{2}\ln(y_{\mathrm{n}}/y_{\mathrm{v}})}{C_{\mu}^{1/4}k_{\mathrm{P}}^{1/2}\kappa}\ \mathrm{vol},$$

$$\iiint_{\mathrm{vol}} -\rho\overline{vw}\,\frac{\partial W}{\partial y}\,\mathrm{d}v = \frac{1}{y_{\mathrm{n}}}\,\frac{\rho\overline{vw}^{2}\ln(y_{\mathrm{n}}/y_{\mathrm{v}})}{C_{\mu}^{1/4}k_{\mathrm{P}}^{1/2}\kappa}\ \mathrm{vol},$$

where y_{n} and y_{v} are height of the near-wall control volume and thickness of the viscous layer respectively. The generation of the wall-normal intensity was assumed negligibly small because the related mean strains were negligible. The linear variation of the turbulent length scale, $L = \kappa y/C_{\mu}^{3/4}$, in the log-law region, together with $\epsilon = k^{3/2}/L$, and the invariant value $\epsilon = 2\mu_{l}k_{\mathrm{v}}/(\rho y_{\mathrm{v}}^{2})$ in the viscous sublayer, allowed the volume-averaged dissipation rate to be determined;

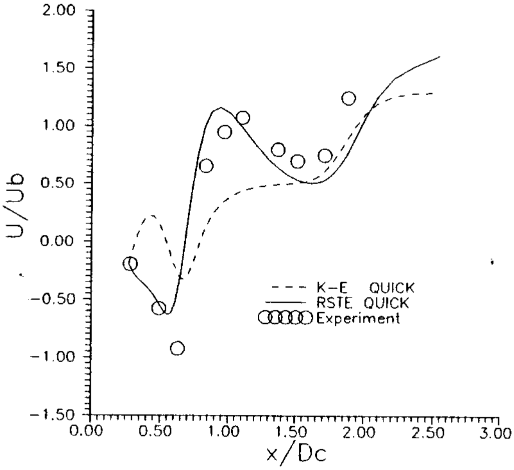

Figure 7. Predicted centreline axial velocity—swirler 1.

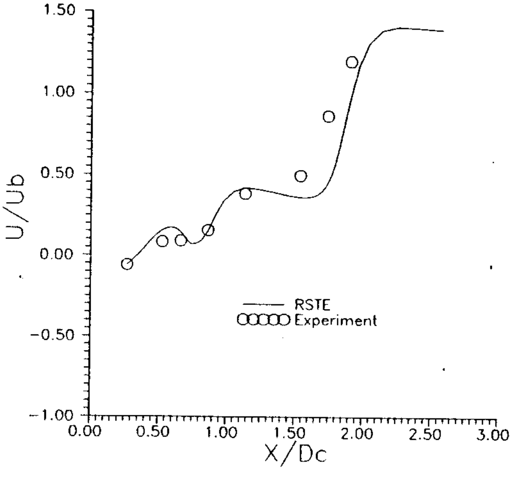

Figure 8. Predicted centreline axial velocity—swirler 2.

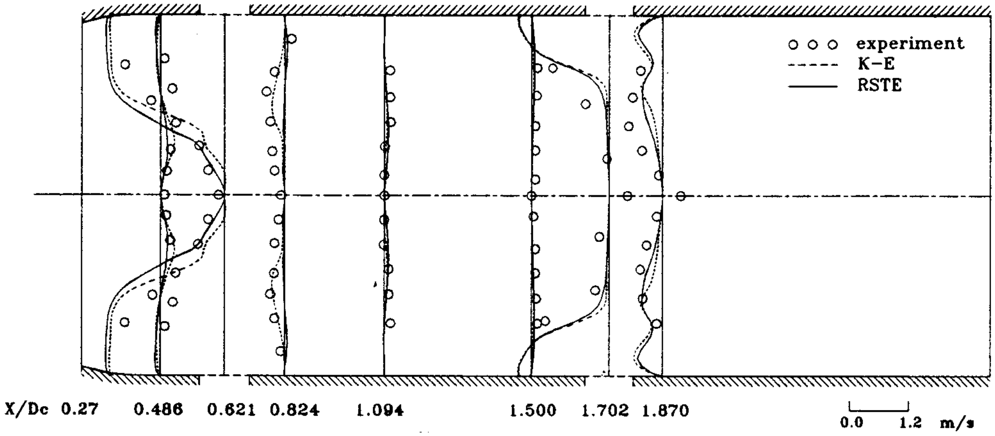

Figure 9. Predicted radial velocity—swirler 1.

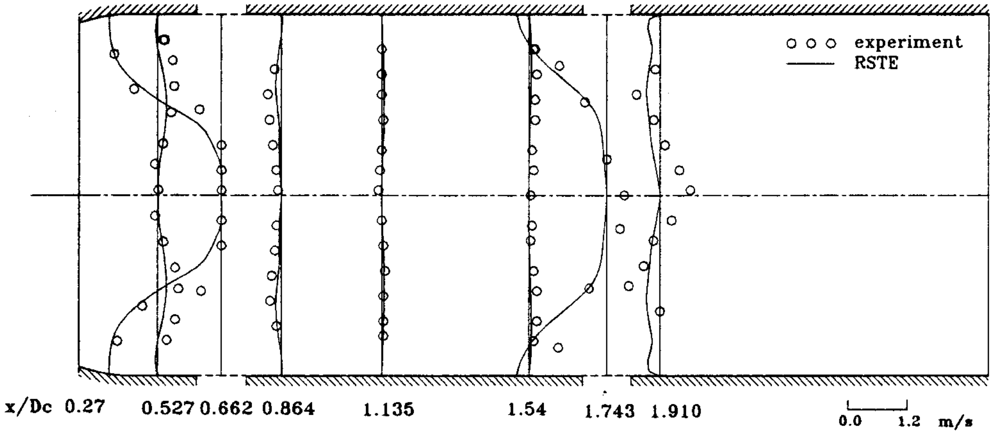

Figure 10. Predicted radial velocity—swirler 2.

details may be found in [14]. This same L-variation was also used to prescribe explicitly the dissipation rate at the near-wall computational node, serving as the boundary condition for inner-field cells.

Previous studies [7] indicated that grid density $49 \times 25 \times 30$ (axial–radial–tangential directions) was adequate in the present flow conditions, therefore, this grid size was adopted in subsequent computations.

4. RESULTS AND DISCUSSIONS

As mentioned earlier, the k–ϵ model is inadequate in this complex physical condition, therefore, the model was applied to swirler 1 only, to give a flavour of the model's performance. Figures 3 and 4 give overall views of the combustor flows for the two swirler cases, predicted with the stress model. The top views show clearly the locations of the radial jets and the swirling flow entering from the left-hand-side of the domain. The intense swirl and jet interaction can be seen from the vector plots. Due to the intense swirl and jet interaction, a high level of swirl momentum is transported to the centreline and the consequence is the formation of the intense swirling vortex along the centreline. The decay of swirling motion causes strong streamline variation of pressure; and consequently leads to a deceleration of its axial velocity, manifesting itself by the appearance of the deep troughs of the velocity profiles along the centreline regions.

Effects of the decay of swirl-induced adverse and favourable pressure gradients can be best observed by reference to the profiles of the axial velocity field, shown in Figures 5 and 6. The predictions show troughs in the centreline regions, $X/D_c = 0.486$ and 0.824, where k–ϵ indicates a higher level of deceleration of the axial velocity in the centreline region, a sign of excessive diffusion and hence higher level of swirl entrainment. Influences of the elevated swirl inlet and turbulence models can be clearly seen from the centreline axial velocity variation shown in Figures 7 and 8. The superior performance of the stress model against the eddy viscosity model is apparent. The influence of the elevated swirl momentum input can be seen from Figures 6 and 8, which show a nearly stagnant region along the centreline near the primary jet. The penetration of the jet was well-represented by the stress models, as are shown in Figures 9 and 10.

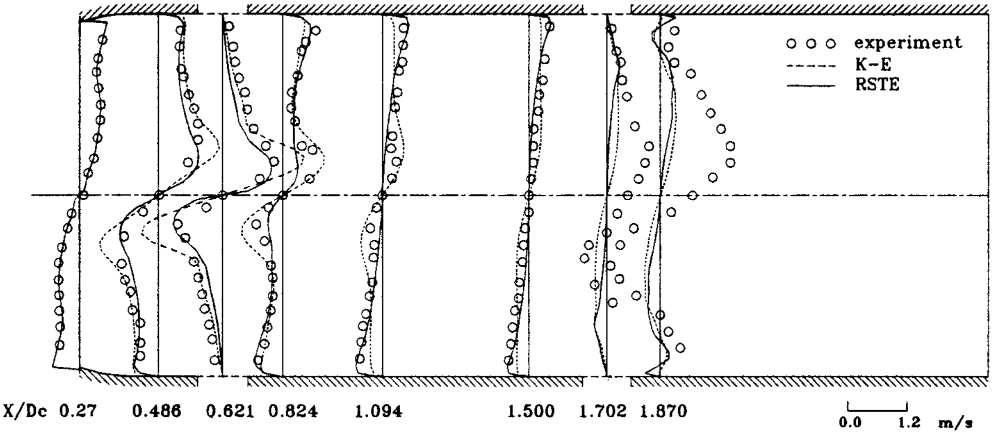

Figure 11. Predicted tangential velocity—swirler 1.

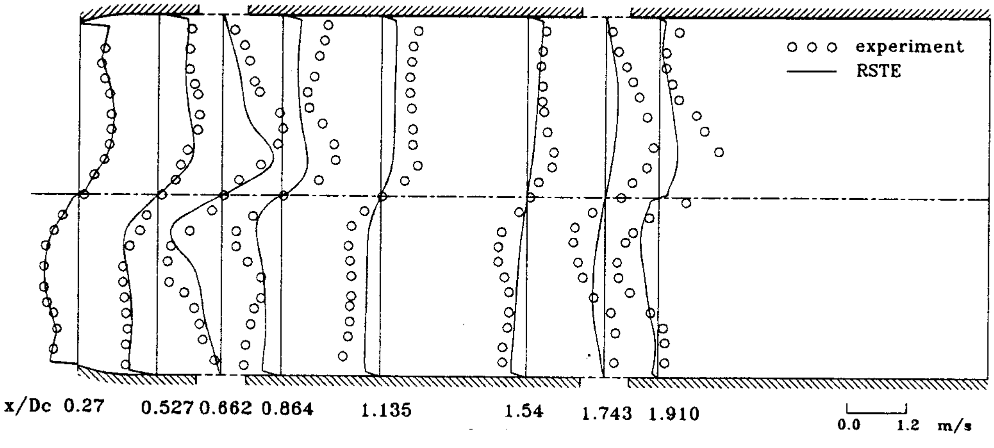

Figure 12. Predicted tangential velocity—swirler 2.

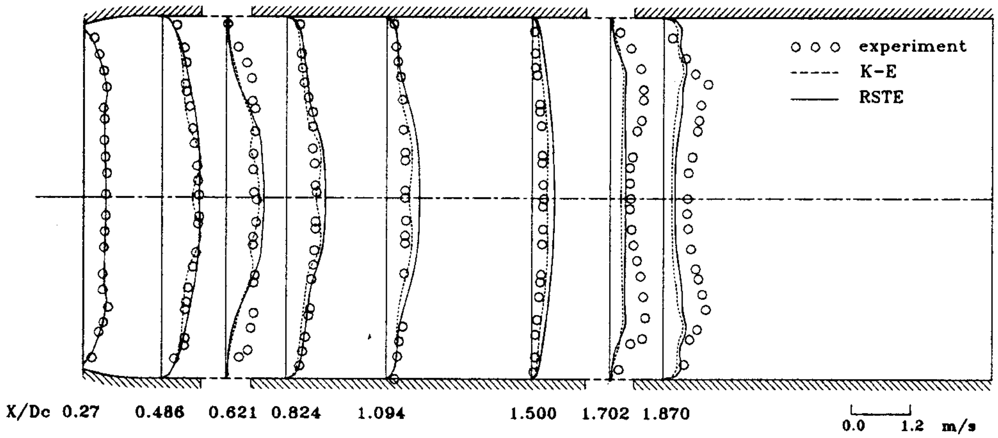

Figure 13. Predicted axial turbulence intensity—swirler 1.

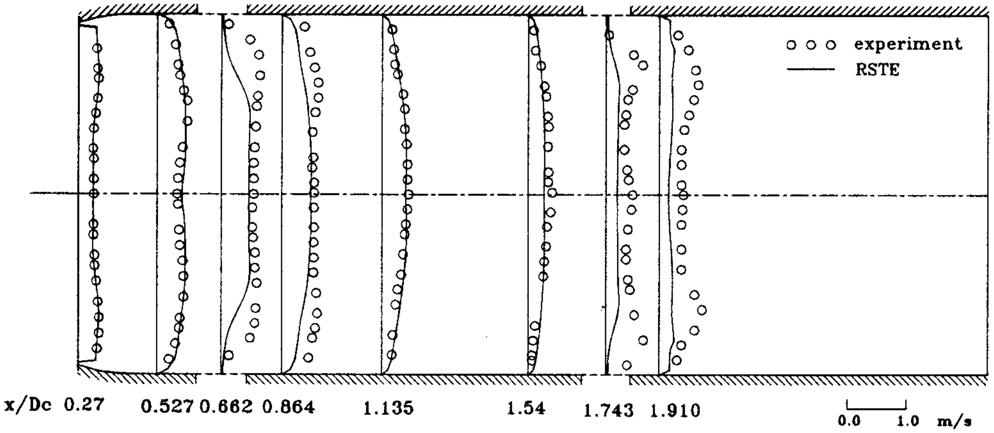

Figure 14. Predicted axial turbulence intensity—swirler 2.

The importance of jet and swirling cross-flow interactions is brought out most dramatically in Figures 11 and 12, which show profiles of swirl velocity. The origin of the severe asymmetric distortions at $X/D_c = 1.702$ and beyond has already been suggested. Attention is rather focused here on the centreline region further upstream. The most prominent feature is the intensely swirling vortex along the centreline due to intense swirl and jet interactions. Both predictions and measurements show large axial variation of swirl velocity leading to a large favourable pressure gradient up to $X/D_c = 0.6$ and a strong adverse gradient thereafter. It is this feature that is responsible for the U-velocity troughs clearly seen in Figures 5 and 6. The gradual return to solid body rotation motion of the swirl profile is also best reproduced by the stress model. k–ϵ predictions, however, displayed a higher level of swirl, and hence, or consequently, a stronger adverse pressure gradient, as was shown in the axial velocity profiles.

Since no experimental data are available for shear stresses, it is appropriate to consider the normal stresses, for it is these quantities that primarily determine levels of shear stresses, and hence the mean flow features. Comparisons between normal stress profiles are shown in Figures 13–18. Here, contrast with experimental data is possible. Of particular interest is the level of $\overline{v^2}$, for this is especially influential in relation to the shear stresses. Figures 15 and 16

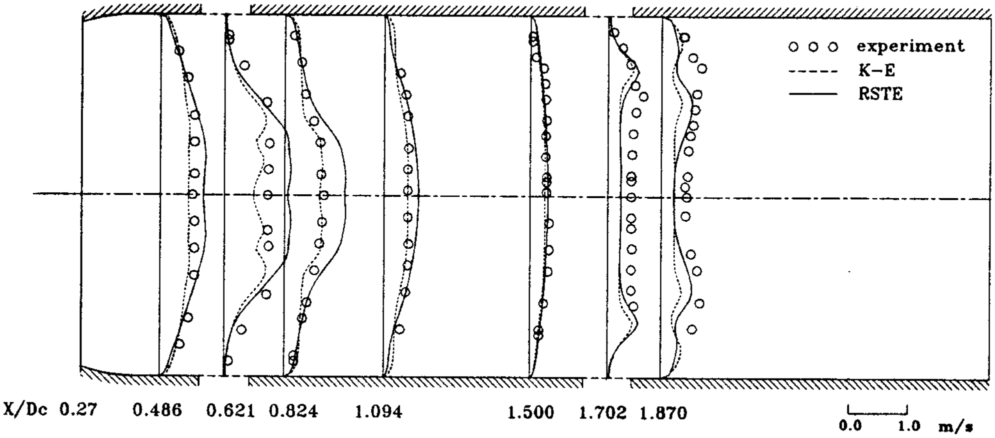

Figure 15. Predicted radial turbulence intensity—swirler 1.

show that stress model predicts, in contrast to the experimental data, high levels of $\overline{v^2}$ at $X/D_c = 0.486$, 0.621 and 0.824 along the centreline regions, exceeding those of the measurements. This observation reveals that the predicted level of shear stress $\overline{uv}$ at this region can be too high, and is consistent with the fast recovery of the predicted axial jet. The stress model's predicting early return to the solid body rotation profiles of the intense swirling vortex core can also be attributed to the higher levels of $\overline{vv}$ and $\overline{ww}$, shown in Figures 17 and 18, predicted by the model.

5. CONCLUSIONS

Computational studies were applied to can-type gas turbine combustor model flows. The amount of fluid and hence swirl momentum transported from the swirler into the combustor interior was large, leading to a very strong interaction between the dilution jets and swirling cross-flow. Due to the intense swirl and jet interaction, a high level of swirl momentum is

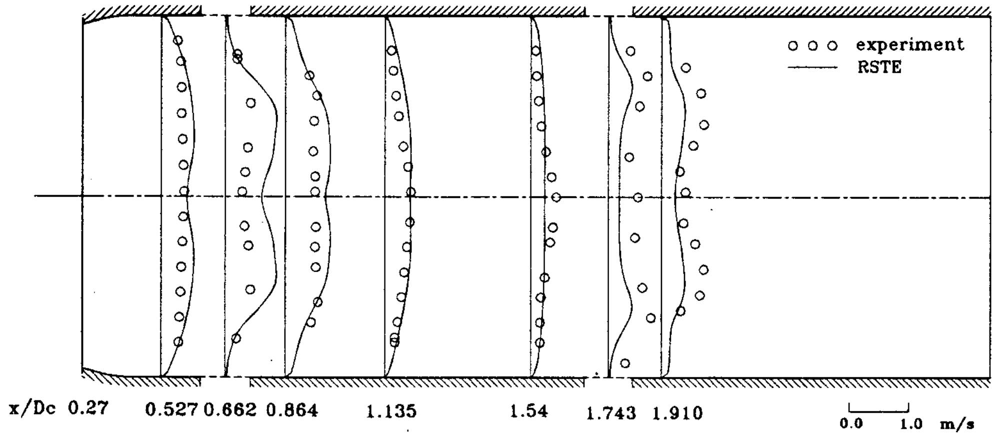

Figure 16. Predicted radial turbulence intensity—swirler 2.

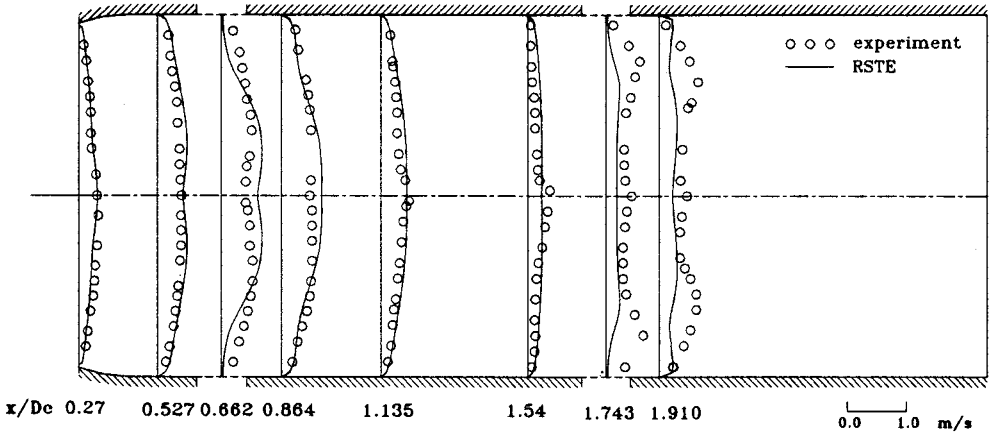

Figure 17. Predicted tangential turbulence intensity—swirler 1.

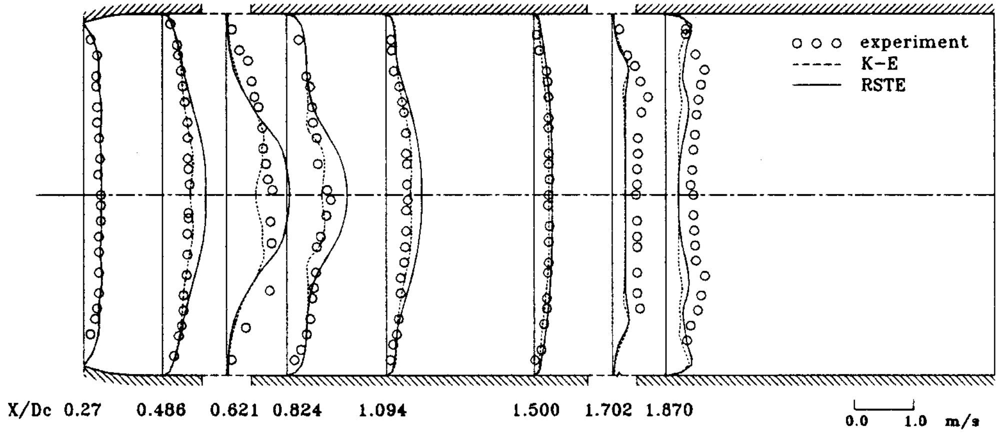

Figure 18. Predicted tangential turbulence intensity—swirler 2.

transported to the centreline and the consequence is the formation of the intense swirling vortex along the centreline. The decay of swirling motion causes strong streamline variation of pressure; and consequently leads to a deceleration of its axial velocity, manifesting itself by the appearance of the deep troughs of the velocity profiles along the centreline regions. Gross flow features, such as the decay of the axial jets after the impingement of the radial primary jets and the gradual return to solid body rotation motion of the swirl profiles, were all captured by the stress model.

ACKNOWLEDGMENTS

This research was supported by National Science Council of Taiwan under grant NSC-840401-E-007-009 and the computational facilities were provided by the National Centre for High Performance Computing of Taiwan, which the authors gratefully acknowledge.

REFERENCES

1. F. Boysan, W.H. Ayers, J. Swithenbank and Z. Pan, 'Three dimensional model of spray combustion in gas turbine combustors', *J. Energy*, **6**, 368–375 (1982).
2. A.S. Green and J.H. Whitelaw, 'Isothermal models of gas turbine combustors', *J. Fluid Mech.*, **126**, 399–412 (1983).
3. J.J. McGuirk and J.M.L.M. Palma, 'The flow inside a model gas turbine combustor: calculations', *Trans. ASME J. Eng. Gas Turbine Power*, **115**, 594–602 (1993).
4. C.H. Priddin and J. Coupland, 'Impact of numerical methods on gas turbine combustor design and development', in R.M.C. So, J.H. Whitelaw and H.C. Mongia (eds.), *Calculation of Turbulent Reactive Flows*, ASME, New York, 1986, pp. 335–348.
5. W. Shyy, W.M. Correa and M.E. Braaten, 'Computation of flow in a gas turbine combustor', *Combust. Sci. Technol.*, **58**, 97–117 (1988).
6. C.A. Lin and M.A. Leschziner, 'Computation of three-dimensional injection into swirling flow with second-moment closure', *6th Int. Conf. on Numerical Methods in Laminar and Turbulent Flows*, Swansea, UK, 1989, pp. 1711–1725.
7. C.A. Lin and C.M. Lu, 'Modelling three-dimensional gas turbine combustor model flow using second-moment closure', *AIAA J.*, **32**, 1416–1422 (1994).
8. M.M. Gibson and B.E. Launder, 'Ground effects on pressure fluctuations in the atmospheric boundary layer', *J. Fluid Mech.*, **86**, 491–511 (1978).
9. T.J. Craft and B.E. Launder, 'Computation of impinging flows using second-moment closures', *Proc. 8th Symp. in Turbulent Shear Flows*, Technical University of Munich, Munich, Germany, 1991, pp. 851–856.
10. S.V. Patankar and D.B. Spalding, 'A calculation procedure for heat mass momentum transfer in three-dimensional parabolic flow', *Int. J. Heat Mass Transf.*, **15**, 1787–1806 (1972).
11. B.P. Leonard, 'A stable and accurate convective modelling procedure based on quadratic upstream interpolation', *Comp. Methods Appl. Mech. Eng.*, **19**, 59–98 (1979).
12. A.K. Gupta, D.G. Lilley and N. Syred, *Swirl Flows*, Abacus Press, 1984.
13. P. Koutmos, 'An isothermal study of gas turbine flow', *Ph.D. Thesis*, University of London, London, 1989.
14. B.E. Launder, 'Low Reynolds number turbulence near walls', *Rep TFD/86/4*, Department of Mechanical Engineering, UMIST, UK, 1986.